

EXTENDED HCN AND HCO⁺ EMISSION IN THE STARBURST GALAXY M82

P. SALAS AND G. GALAZ

Instituto de Astrofísica, Facultad de Física, Pontificia Universidad Católica de Chile, Av. Vicuña Mackenna 4860, 782-0436 Macul, Santiago, Chile

D. SALTER, R. HERRERA-CAMUS, AND A. D. BOLATTO

Department of Astronomy and Laboratory for Millimeter-Wave Astronomy, University of Maryland, College Park, MD 20742, USA

A. KEPLEY

National Radio Astronomy Observatory, 520 Edgemont Road, Charlottesville, VA 22903-2475, USA

Draft version August 23, 2021

ABSTRACT

We mapped 3 mm continuum and line emission from the starburst galaxy M82 using the Combined Array for Research in Millimeter-wave Astronomy. We targeted the HCN, HCO⁺, HNC, CS and HC₃N lines, but here we focus on the HCN and HCO⁺ emission. The map covers a field of 1'2 with a $\approx 5''$ resolution. The HCN and HCO⁺ observations are combined with single dish images. The molecular gas in M82 had been previously found to be distributed in a molecular disk, coincident with the central starburst, and a galactic scale outflow which originates in the central starburst. With the new short spacings-corrected maps we derive some of the properties of the dense molecular gas in the base of the outflow. From the HCN and HCO⁺ J = (1 – 0) line emission, and under the assumptions of the gas being optically thin and in local thermodynamic equilibrium, we place lower limits to the amount of dense molecular gas in the base of the outflow. The lower limits are $7 \times 10^6 M_{\odot}$ and $21 \times 10^6 M_{\odot}$, or $\gtrsim 2\%$ of the total molecular mass in the outflow. The kinematics and spatial distribution of the dense gas outside the central starburst suggests that it is being expelled through chimneys. Assuming a constant outflow velocity, the derived outflow rate of dense molecular gas is $\geq 0.3 M_{\odot} \text{ yr}^{-1}$, which would lower the starburst lifetime by $\geq 5\%$. The energy required to expel this mass of dense gas is $(1 - 10) \times 10^{52}$ erg.

Subject headings: galaxies: individual (M82) – galaxies: starburst – galaxies: ISM – ISM: jets and outflows

1. INTRODUCTION

The low-end of the stellar mass function of galaxies is often explained as a consequence of stellar feedback (e.g., Oppenheimer et al. 2010). Continuous energy injection into the interstellar medium (ISM) by stellar feedback influences the way in which star formation carries on. Numerical simulations show that continuous supernovae (SNe) explosions can end up building a coherent galactic wind (e.g., Melioli, de Gouveia Dal Pino, & Geraissate 2013). This wind is capable of carrying ISM material from the central regions of the galaxy to its outer regions, in some cases reaching the intergalactic medium (for a review on galactic winds see Veilleux, Cecil, & Bland-Hawthorn 2005). This process can remove gas from the starburst, providing negative feedback to star formation (Springel & Hernquist 2003; Oppenheimer & Davé 2006). Understanding the role of galactic winds on galaxy evolution requires determining the relative contributions of the different ISM phases to the wind (Veilleux et al. 2009). Of the different ISM phases, the relatively cold and dense molecular gas phase is the one most directly related to star formation. Observations of cold molecular gas in starburst-driven galactic winds are few and are only available for a couple of objects: M82 (Nakai et al. 1987; Loiseau et al. 1990; García-Burillo et al. 2001; Walter et al. 2002; Kepley et al. 2014), NGC253 (Bolatto et al. 2013) and

NGC3628 (Tsai et al. 2012). However, these suggest that the relatively cool molecular gas phase is an important fraction of the wind mass budget.

To study the relative importance of the different ISM components in an outflow we obtained maps of dense gas in one of the closest starburst galaxies with a known starburst-driven wind, M82 ($D = 3.4 \pm 0.2$ Mpc, Dalcanton et al. 2009). Its central starburst covers a region ~ 1 kpc in diameter (O’Connell & Mangano 1978), and hosts an extreme environment as suggested by its high star formation rate of $\sim 9 M_{\odot} \text{ yr}^{-1}$ (Strickland et al. 2004) and infrared luminosity $L_{\text{IR}} \approx 5.6 \times 10^{10} L_{\odot}$ (Sanders et al. 2003). Its proximity and high star formation rate have made it a target for observations covering the whole electromagnetic spectrum. This has permitted to draw a picture of the starburst in great detail. The starburst-driven wind in M82 was first observed by Lynds & Sandage (1963). The outflow presents a bipolar structure, observed in X-rays (Bregman, Schulman, & Tomisaka 1995; Strickland, Ponman, & Stevens 1997; Stevens, Read, & Bravo-Guerrero 2003), optical emission lines (Shopbell & Bland-Hawthorn 1998), CO (Walter et al. 2002), polycyclic aromatic hydrocarbons (PAHs, Engelbracht et al. 2006; Yamagishi et al. 2012), warm H₂ (Veilleux et al. 2009), dust (Roussel et al. 2010), forbidden lines in the IR (Contursi et al. 2013)

and dense molecular gas (Kepley et al. 2014). These observations have shown that the different ISM phases coexist in the wind, with the cold molecular component, traced by CO, dominating the mass and kinetic energy budget of the wind.

In this work we present new continuum and line emission observations of M82 obtained with the Combined Array for Research in Millimeter-wave Astronomy (CARMA). Among them are HCN and HCO⁺ observations with high sensitivity and spatial resolution. The maps of bf Kepley et al. (2014) were the first to reveal HCO⁺ and HCN emission associated with the starburst-driven outflow in M82 thanks to the high sensitivity of the Green Bank Telescope (GBT). We combine our HCN and HCO⁺ maps with the GBT data to recover the missing large scale flux resolved out by CARMA. The use of new CARMA data along the previously published GBT observations results in maps with a factor of 2 better angular resolution which enables to study the dense gas in the galactic wind with greater detail.

In §2 we present the new CARMA observations and how these were combined with the GBT observations. Then in §3 we determine the amount of dense gas present in the outflow from the resulting maps. Finally, in §4 we give a summary of our main findings.

2. OBSERVATIONS AND DATA REDUCTION

2.1. CARMA observations

We observed M82 in the 3 mm band using CARMA¹ in its D configuration (baselines 11-150 m) during April and May 2012. We observed a 7 point mosaic centered on $\alpha = 09^{\text{h}}55^{\text{m}}53.00^{\text{s}}$, $\delta = +69^{\circ}40'47''$ (J2000), the radio center of this galaxy. This mosaic covers a circular region of $\sim 1'.2$ in diameter. The correlator was tuned to have 16×250 MHz windows with a 3.125 MHz spectral resolution. This corresponds to a velocity coverage of ~ 770 km s⁻¹ with 10.5 km s⁻¹ resolution. Eleven windows were used to measure the continuum emission and the remaining 5 were centered over the molecular lines shown in Table 1. Observations were reduced using *MIRIAD* data reduction software (Sault et al. 1995). Mars was used as a primary flux calibrator. Passband solutions were derived by observing 0927+390, and gain solutions observing 0836+710 (or 0841+708 by its B1950 name). A linear baseline was removed from the windows with spectral lines. The baseline was determined from the line free windows and channels. The average synthesized beam of the final cubes is $\sim 5''.2 \times 4''.9$ ($6'' \approx 102$ pc) and the average channel rms is 44 mK (≈ 7.4 mJy beam⁻¹). A summary of the cube properties is presented in Table 1.

2.2. Short-spacings correction

The shortest baseline of 11 m makes the telescope blind to structures larger than $\sim 50''$. To correct for the

¹ Support for CARMA construction was derived from the states of California, Illinois, and Maryland, the James S. McDonnell Foundation, the Gordon and Betty Moore Foundation, the Kenneth T. and Eileen L. Norris Foundation, the University of Chicago, the Associates of the California Institute of Technology, and the National Science Foundation. Ongoing CARMA development and operations are supported by the National Science Foundation under a cooperative agreement, and by the CARMA partner universities.

TABLE 1
CARMA OBSERVATIONS SUMMARY

Molecule	Frequency ^a (GHz)	Obs. beam (" × ")	rms (mK)	$n_{\text{crit}}^{\text{b}}$ ($\times 10^5$ cm ⁻³)
HCN(1 – 0)	88.63	5.5×5.2	43	1.9×10^6
HCO ⁺ (1 – 0)	89.18	5.5×5.2	48	2.1×10^5
HNC(1 – 0)	90.66	5.3×4.9	43	3.5×10^5
HC ₃ N(10 – 9)	90.98	5.4×5.0	40	$3.6 \times 10^{6\text{c}}$
CS(2 – 1)	97.98	4.9×4.7	40	2.7×10^4

^a Spectral line frequencies were taken from the Spectral Line Atlas of Interstellar Molecules (SLAIM) (Available at <http://www.splatalogue.net>). (F. J. Lovas, private communication, Remijan et al. 2007)

^b Critical density $n_{\text{crit}} \approx A_{ul} / \sum_i \langle v\sigma_{ui} \rangle$ where A_{ul} is the Einstein coefficient and $\langle v\sigma_{ul} \rangle$ is the collisional rate. Critical densities were computed for $T = 50$ K. Collisional rates and Einstein coefficients were taken from the Leiden Atomic and Molecular Data base (LAMDA, Schöier et al. 2005).

^c Collisional rates not available for HC₃N. This value was taken from Aladro et al. (2011a) which uses $T = 90$ K.

negative bowl in visibility amplitude produced by the lack of short spacings we used GBT HCN and HCO⁺ observations (Kepley et al. 2014). Images were combined in spatial frequency space using *MIRIAD*'s *IMMERGE*. This method yields similar results to other missing short-spacings correction methods (Stanimirovic 2002). The flux scaling between GBT and CARMA data was determined in an annulus of 4 – 33 kλ, corresponding roughly to the dish size of the GBT and the shortest baseline in the interferometer array. Flux scaling factors were 0.376 and 0.4 for HCN and HCO⁺ respectively. The short spacing corrected channel rms is 44 mK ($= 7.2$ mJy beam⁻¹) for HCN and 42 mK ($= 7.0$ mJy beam⁻¹) for HCO⁺. The integrated line brightness of the short-spacing corrected maps is different from those presented in Nguyen-Q-Rieu et al. (1989) by 2% for HCN and 13% for HCO⁺.

The remaining observations presented in this work, 3 mm continuum, HNC, CS and HC₃N, were not corrected for missing short-spacings.

3. RESULTS

3.1. 3 mm continuum

The 3 mm continuum emission from the central region of M82 is dominated by optically thin free-free emission (Carlstrom & Kronberg 1991), which is produced by ionized gas ($\sim 10^4$ K) present in H⁺ regions. This makes the 3 mm continuum emission from M82 a good tracer of sites of recent star formation. Hence, the extent of the 3 mm continuum should be similar to that of the central starburst.

The new 3 mm continuum map obtained with CARMA is shown in Fig. 1. In the same figure we show the H α emission from M82 as observed with the Hubble Space Telescope Advanced Camera for Surveys (HST/ACS, Mutchler et al. 2007), and the reference CO(1 – 0) map of Walter et al. (2002). The CO map was obtained with a combination of Owen Valley Radio Observatory plus IRAM 30 m data. A visual comparison between the HST image and the 3 mm continuum from this work (Fig. 1) reveals that the peaks of the 3 mm continuum correspond to regions of high dust opacity in the H α image. The continuum disk has a minor axis of $\approx 7''$, similar to

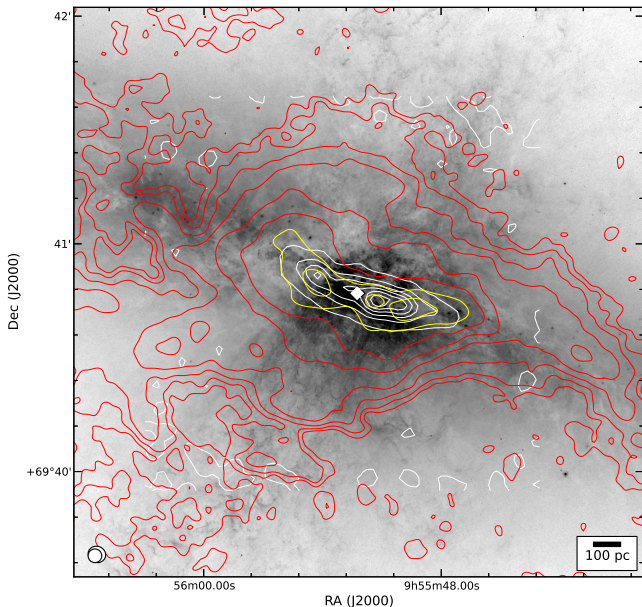


FIG. 1.— 3 mm continuum emission from the central region of M82 (white contours) overlaid on a $H\alpha$ emission image from the HST/ACS (inverted logarithmic gray scale, Mutchler et al. 2007) and CO $J = 1 - 0$ moment 0 map (red contours: outflow; yellow contours: molecular disk Walter et al. 2002). The white diamond shows the location of the galactic center as defined by the $2.2 \mu\text{m}$ peak (Dietz et al. 1989). The continuum contours start at 3σ , with $\sigma = 21 \text{ mK}$. Each increment is 6σ . The CARMA beam of the observations presented in this work is shown as the large white circle on the lower left corner. The smaller circle shows the beam of the CO observations ($3''.6 \times 3''.6$, Walter et al. 2002)

the number density scale height of the stellar clusters in M82 ($\approx 9''$, Lim, Hwang, & Lee 2013). The major axis of the continuum disk is of $\approx 30''$. The extent of the continuum is also similar to that of the molecular disk as observed in the CO map. This motivates us to define the spatial extent of the molecular disk as a combination of the continuum disk presented here, and the CO molecular disk (Walter et al. 2002).

The continuum map is similar to that found in previous studies (Carlstrom 1989; Carlstrom & Kronberg 1991; Brouillet & Schilke 1993; Neininger et al. 1998). In their work Brouillet & Schilke (1993) report a total flux of $\approx 0.45 \text{ Jy}$ for the South-West portion of the galaxy. In our maps the total integrated flux over the disk is $\approx 0.50 \pm 0.03 \text{ Jy}$. The total continuum flux is in agreement with the single dish flux reported by Jura, Hobbs, & Maran (1978, $\approx 0.54 \pm 0.08 \text{ Jy}$).

3.2. HCN and HCO^+ line emission

Channel maps corrected for missing short spacings are presented in Figs. 2 and 3. These show the location of extraplanar emission extending below and above the starburst disk. For HCN, in the velocity range $121 - 343 \text{ km s}^{-1}$ emission extends above and below the molecular disk. The situation is similar for HCO^+ , for which in the velocity range $114 - 366 \text{ km s}^{-1}$ we see emission more extended than the molecular disk along its minor axis. This emission comes from regions near the start of the outflow as observed in CO and $H\alpha$ (see Fig. 1). This suggests that the extraplanar emission extending above and below the molecular disk might be entrained in the galactic wind. The extraplanar HCO^+

emission had been previously associated with the galactic wind in M82 (Kepley et al. 2014). Here we extend this association to the HCN emission as well.

The molecular disk spans a velocity range $52 - 387 \text{ km s}^{-1}$, and its kinematics have been discussed in depth by Brouillet & Schilke (1993) for HCN and Seaquist et al. (1998) for HCO^+ . The extraplanar emission follows the rotation of the molecular disk. We find no observable counterpart to the chimney traced by $\text{SiO}(2 - 1)$ (García-Burillo et al. 2001) in the channel maps. The SiO chimney appears at a velocity of 150 km s^{-1} to the East of M82 center, that is blueshifted with respect to the disk velocity at the base of the chimney.

Using the velocity ranges defined above for the disk and extraplanar emission we construct moment 0 maps using a masked moment method as described in Dame (2011). In this method the data cubes are first convolved with a larger beam to smooth out small scale variations. Then a threshold is applied to the smoothed data to create a mask that is used to construct the moment 0 maps. For the convolution we use a Gaussian twice the CARMA beam ($11''$) in the RA-DEC plane and two times the velocity resolution (21 km s^{-1}) in the velocity axis. We use a threshold of 2.5 times the convolved map rms to recover emission. This method is good at recovering faint emission that is distributed similarly to the bright emission, but is biased against isolated faint emission (Regan et al. 2001; Helfer et al. 2003). The moment 0 maps are presented in Figs. 4 and 5, for the CARMA data alone as well as the cubes corrected for missing short spacings. In the moment 0 maps we apply a 3σ cut to separate emission from noise. The differences between the short spacings-corrected data and the interferometric data alone are evident and we caution the reader not to directly compare both. A comparison based on the CARMA data alone shows that the HCO^+ emission is the most extended outside the plane, then follows HCN. Emission from HCN and HCO^+ is slightly more extended than that of the 3 mm continuum (Fig. 1). In Fig. 5 we also include 14 regions which are later used to estimate the amount of molecular gas mass outside the central starburst. These regions have sizes of $7''.5$, chosen to sample regions slightly larger than the synthesized beam. These regions are located where the extraplanar emission extends at least $5''$ above or below the central starburst.

The short spacings-corrected moment 0 maps show the presence of the extended component (Fig. 5). Near the edge of the molecular disk the HCN and HCO^+ emission show a chimney like structure. Similar to that observed in [NeII] (Achtermann & Lacy 1995) and 5 GHz continuum (Wills et al. 1999). The extended HCO^+ emission is coincident with the dark lane in the Eastern edge of the 3 mm continuum in Fig. 1 (also in Fig. 5 of Ohyama et al. 2002).

The HCN and HCO^+ emission are not spatially coincident in various regions outside the central starburst. In regions 1, 2, 4 and 5 emission from HCO^+ is not observed. The noise level in these regions on both maps are similar. This implies that the observed differences are due to different emission levels. If we take the 3σ limit for the missing molecule, the non-detection of HCO^+ emission implies HCN/HCO^+ ratios ≥ 1.5 . The non-detection of

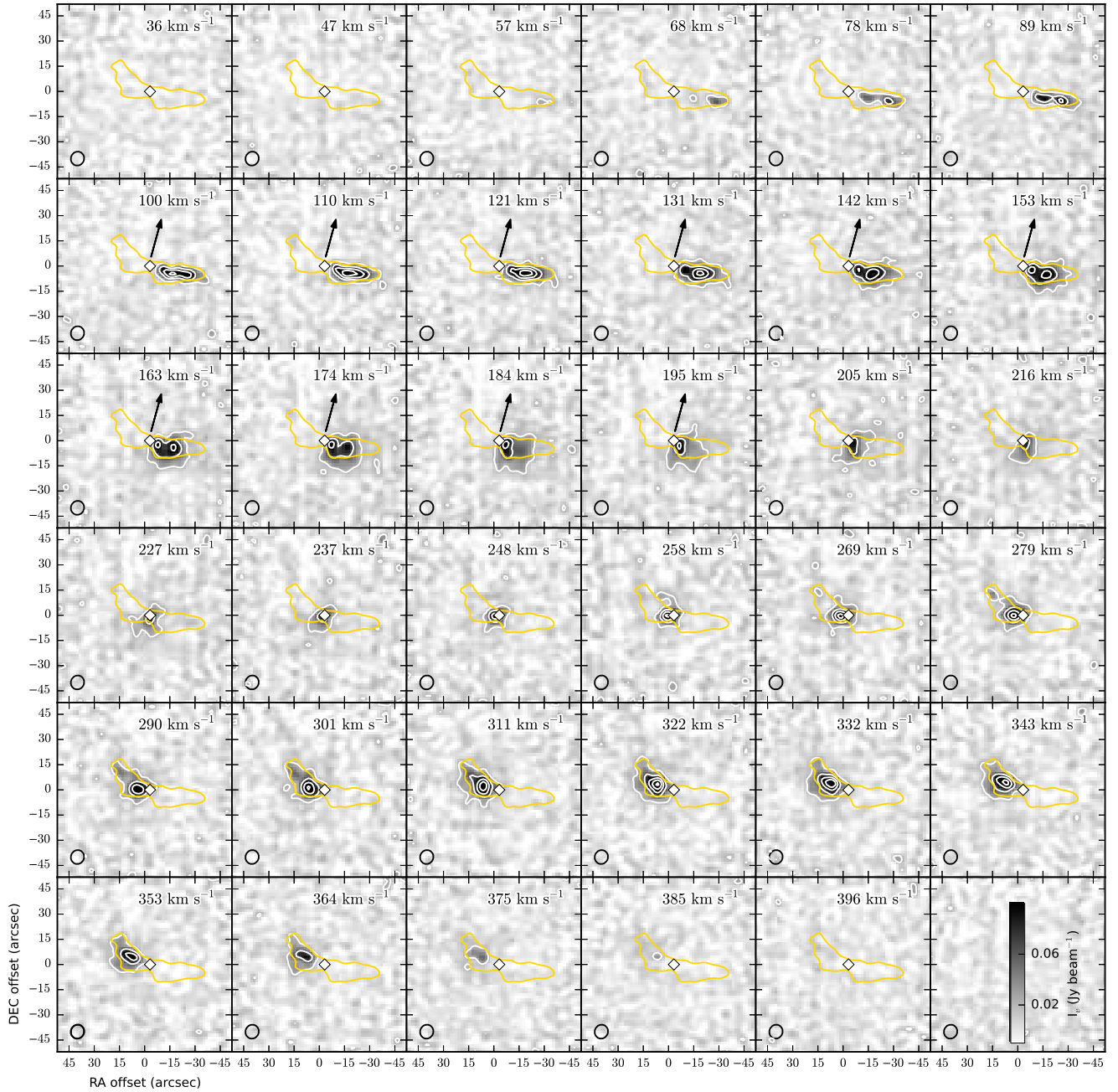


FIG. 2.— HCN channel map. The radio velocity with respect to the local standard of rest is shown in the upper right corner of each panel. The white diamond marks the position of the galaxy center ($2.2 \mu\text{m}$ peak Dietz et al. 1989), and the arrow in some of the panels marks the location of the SiO(2 – 1) chimney (García-Burillo et al. 2001). The interferometer beam is shown in the lower left panel. Contours start at 3σ with 12σ increments. $1\sigma = 7.1 \text{ mJy beam}^{-1} = 43 \text{ mK}$.

HCN emission in regions 8, 9 and 10 implies HCN/HCO⁺ ratios ≤ 0.75 .

The most extended component observed in HCN reaches a projected distance relative to the $2.2 \mu\text{m}$ peak of $\approx 22''$, just above region 5 in Fig. 5. To the south of region 2 the projected distance is $\approx 21''$. For HCO⁺ the most extended emission comes from a projected distance of $\approx 31''$, to the north of region 14, and $\approx 37''$, to the south of region 9. The prominent extra-planar emission from HCO⁺ (regions 9 and 14 in Fig. 5) is spatially coincident with the dust lane that passes near the center

of M82 (see Fig. 1).

3.3. Other detected molecules

CS, HNC and HC₃N emission comes from within the molecular disk. HC₃N is detected in the North-East lobe, where transitions up to $J = 28$ have been detected from the same molecule (Aladro et al. 2011b). The lack of CS and HNC emission outside the molecular disk could be due to a lower signal-to-noise ratio, as their emission is fainter than that of HCN and HCO⁺.

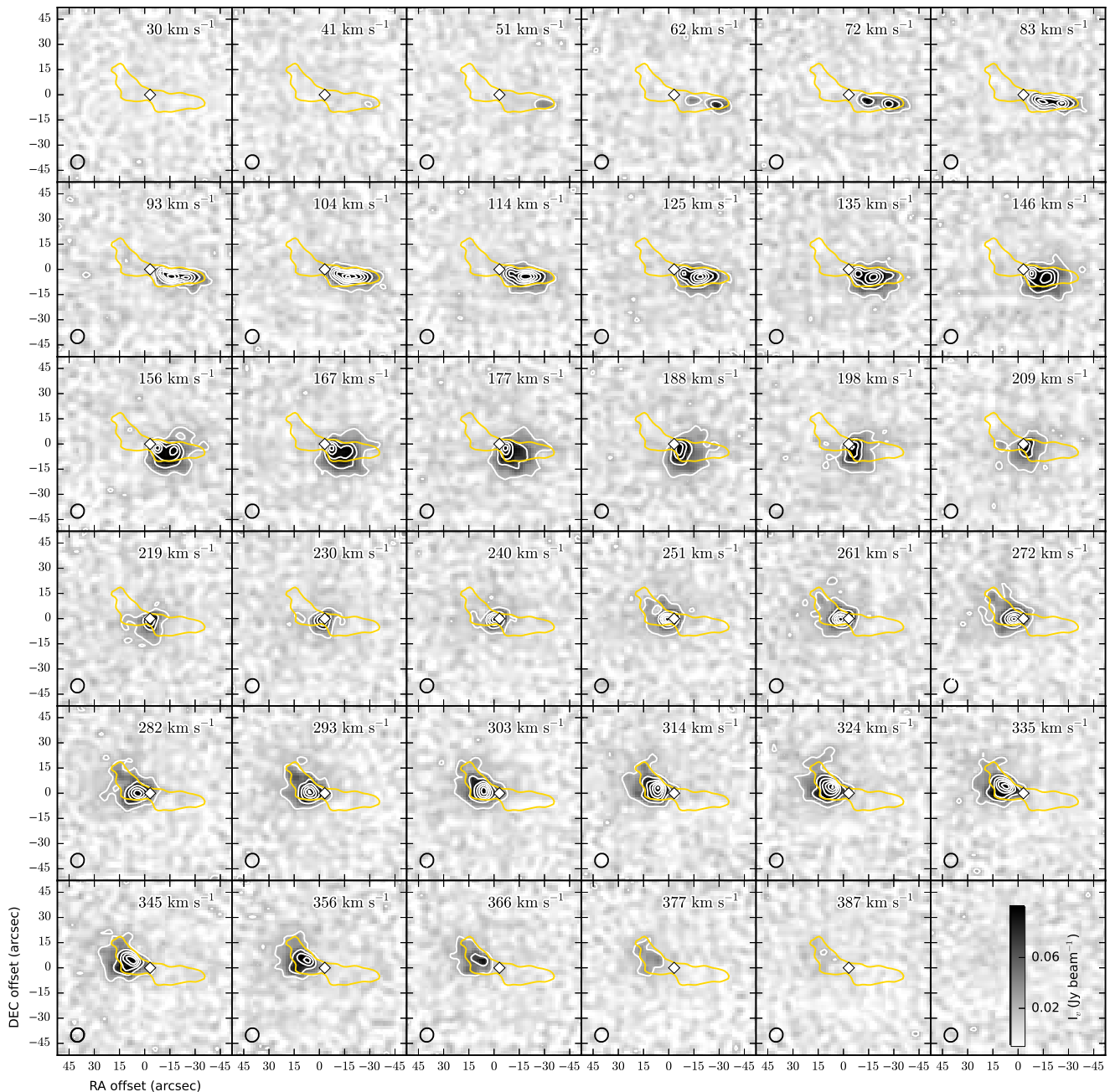


FIG. 3.— HCO^+ channel map. The radio velocity with respect to the local standard of rest is shown in the upper right corner of each panel. The white diamond marks the position of the galaxy center ($2.2 \mu\text{m}$ peak Dietz et al. 1989). The interferometer beam is shown in the lower left panel. Contours start at 3σ with 12σ increments. $1\sigma = 7.0 \text{ mJy beam}^{-1} = 43 \text{ mK}$.

3.4. SFR from 3 mm continuum

The 3 mm continuum in M82 is $\geq 60\%$ due to free-free emission (Carlstrom & Kronberg 1991). Using the observed 3 mm continuum we derive a star formation rate (SFR) from (e.g., Murphy et al. 2011)

$$\left(\frac{\text{SFR}^{\text{ff}}}{M_{\odot} \text{ yr}^{-1}} \right) = 4.6 \times 10^{-28} \times \left(\frac{T_e}{10^4 \text{ K}} \right)^{-0.45} \left(\frac{\nu}{\text{GHz}} \right)^{0.1} \left(\frac{L_{\nu}^{\text{ff}}}{\text{erg Hz}^{-1} \text{ s}^{-1}} \right). \quad (1)$$

Here T_e is the electron temperature and L_{ν}^{ff} the luminosity due to free-free emission. We adopt an electron temperature of 5000 K, derived from radio recombination lines observations (Puxley et al. 1989). If we consider that the contribution to free-free emission is 60 – 100% (Carlstrom & Kronberg 1991), then the SFR rate is $4 - 7 M_{\odot} \text{ yr}^{-1}$. This value is 20% lower than the IR luminosity derived SFR presented by Strickland et al. (2004). The lower value presented here could be attributed to the smaller region being probed with the 3 mm continuum.

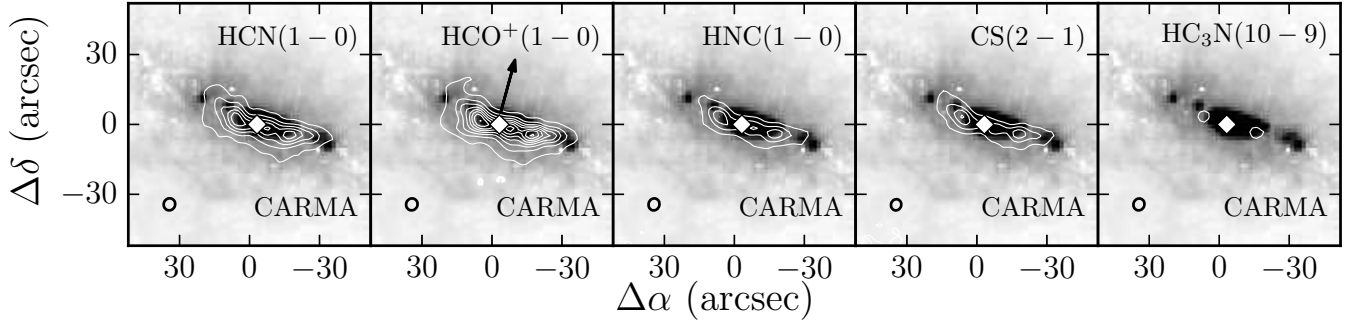


FIG. 4.— Integrated intensity (moment 0) maps of line emission (solid contours) overlaid on a map of $\text{H}_2 v = 1 - 0 \text{ S}(1)$ emission (inverted gray scale, Veilleux et al. 2009). The line emission maps were obtained with the CARMA telescope and have not been corrected for missing short spacings. The arrow on the HCO^+ map shows the location of the SiO chimney (García-Burillo et al. 2001). Contours start at 3σ and increment by 6σ , with σ the moment 0 map rms. $\sigma_{\text{HCN}} \approx 2.5 \text{ K km s}^{-1}$, $\sigma_{\text{HCO}^+} \approx 2.7 \text{ K km s}^{-1}$, $\sigma_{\text{HNC}} \approx 2.5 \text{ K km s}^{-1}$, $\sigma_{\text{CS}} \approx 2.3 \text{ K km s}^{-1}$, $\sigma_{\text{HC}_3\text{N}} \approx 1.8 \text{ K km s}^{-1}$. The CARMA beam is shown on the lower left corner of each panel.

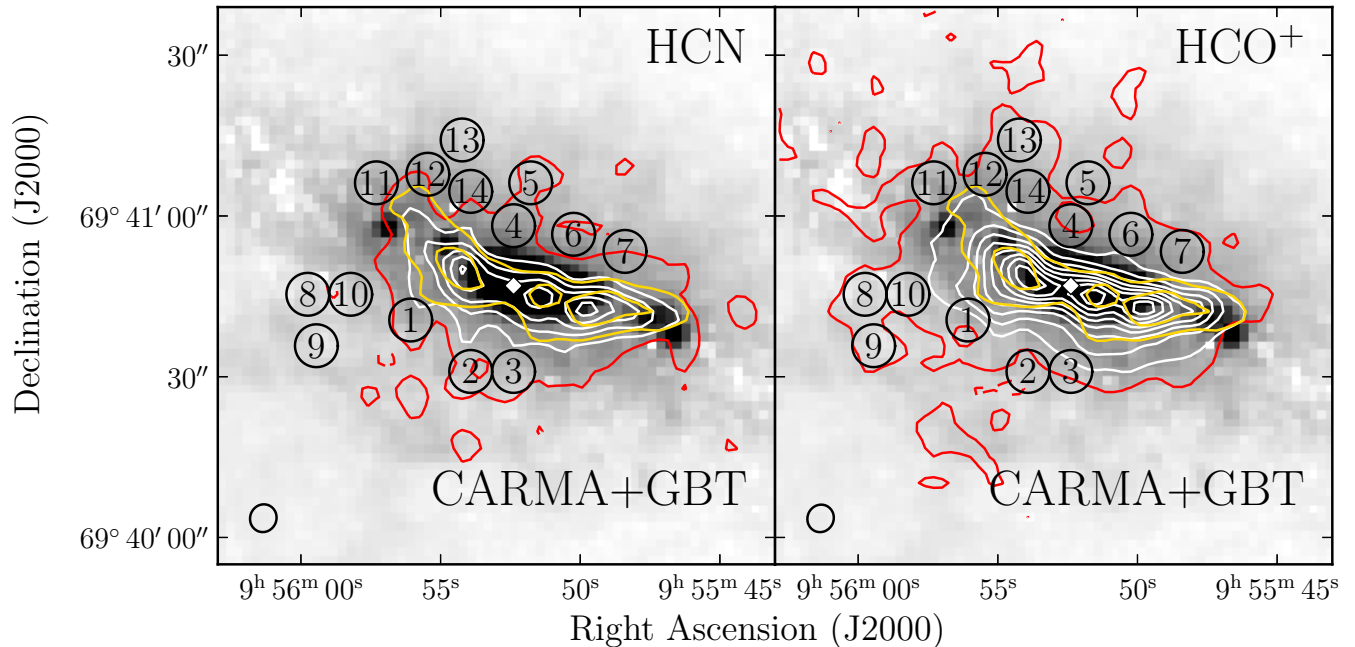


FIG. 5.— Short spacings-corrected integrated intensity (moment 0) maps of HCN and HCO^+ emission (solid contours) overlaid on a map of $\text{H}_2 v = 1 - 0 \text{ S}(1)$ emission (inverted gray scale, Veilleux et al. 2009). Emission associated with the central starburst is shown in *white* and that associated with the starburst-driven wind is shown in *red*. The CO molecular disk is shown as yellow contours (Walter et al. 2002) and the galaxy center defined by the $2.2 \mu\text{m}$ peak as a white diamond (Dietz et al. 1989). The CARMA beam is shown in the lower left corner of each panel. Contours start at 3σ and increment by 6σ , with σ the moment 0 map rms. $\sigma_{\text{HCN}} = 2.5 \text{ K km s}^{-1}$, $\sigma_{\text{HCO}^+} = 2.5 \text{ K km s}^{-1}$.

3.5. Dense molecular gas mass outside the central starburst

To determine the column density we use the regions shown in Fig. 5. The area-averaged velocity-integrated brightness temperatures inside these regions are given in Table 2. Velocity-integrated line fluxes over the whole molecular disk and outflow are given in Table 3. For the outflow a velocity range of $115 - 367 \text{ km s}^{-1}$ is used, and for the molecular disk $50 - 390 \text{ km s}^{-1}$.

We cannot determine the optical depth nor the excitation temperature of the gas as we lack information about higher J transitions, hyperfine structure transitions or isotopic line ratios for the observed molecules we cannot determine the optical depth nor the excitation temper-

ature of the gas. Therefore we assume that the gas is optically thin and in local thermodynamic equilibrium (LTE). While this assumption is not likely to hold in the central starburst region of M82, it might be appropriate for the gas in a wind (Weiß et al. 2005).

The overall effect of the optically thin and LTE assumptions is that the computed column densities are lower limits. Studies using multiple transitions of HCN and HCO^+ suggests optical depths close to unity ($\tau \sim 1$, Nguyen et al. 1992; Naylor et al. 2010) in the central starburst. A greater than unity optical depth would increase the column density. Deviations from LTE are expected if the density is lower than its critical value. The conditions in the outflow are similar to those of the low excitation component in the central starburst

TABLE 2
AVERAGE $\int T_b dv$ OUTSIDE THE
CENTRAL STARBURST IN M82.

Region	$\int T_{b,\text{HCN}} dv$ (K km s ⁻¹)	$\int T_{b,\text{HCO}^+} dv$ (K km s ⁻¹)
1	15 ± 4	24 ± 11 [†]
2	11 ± 2	10.0 ± 0.2 [†]
3	14 ± 3	19 ± 8 [†]
4	14 ± 3	12 ± 3 [†]
5	12 ± 3	9 ± 0.3 [†]
6	8 ± 1 [†]	13 ± 3
7	9 ± 2 [†]	16 ± 2
8	...	13 ± 1
9	...	10 ± 1
10	...	15 ± 2
11	8 ± 2 [†]	14 ± 3
12	9 ± 2 [†]	17 ± 4
13	...	14 ± 1
14	10 ± 1 [†]	13 ± 2

[†] Regions filled less than 50%.

(Weiß et al. 2005). The density in the outflow inferred from CO studies is $\approx 10^3 \text{ cm}^{-3}$, which would imply that the HCN and HCO⁺ lines are sub-thermally excited. In the case of sub-thermal excitation the LTE assumption provides a lower limit to the true column density.

Under the optically thin and LTE assumptions the column density, N , is given by (e.g., Nguyen-Q-Rieu et al. 1989)

$$N = \frac{3k_B}{8\pi^3\nu\mu^2S} \frac{Q(T_{\text{ex}})}{e^{-E_u/T_{\text{ex}}}} \int T_b dv. \quad (2)$$

Here k_B is the Boltzmann constant, ν the transition frequency, μ the molecule permanent dipole moment, S the line strength, Q the partition function, T_{ex} the excitation temperature, E_u the upper state energy and T_b the line brightness temperature in temperature units. We adopt $\mu^2 S$ to be 8.91135 D² for HCN (Remijan et al. 2007) and 15.21 D² for HCO⁺ (Yamaguchi et al. 1994).

The second major uncertainty in our column density calculation comes from the poorly known gas temperature. Multi transition analysis of the physical conditions in the molecular disk of M82 suggests that the excitation temperature of the HCN and HCO⁺ emitting gas is greater than 40 K (Naylor et al. 2010). Outside the molecular disk, the gas temperatures seem to be above 30 K and below 120 K (Weiß et al. 2005). We adopt a temperature range of 30–120 K to compute the column densities. The column density changes by 70% between the extremes of this temperature range. The column densities derived under these assumptions are presented in Table 4. As the interferometer beam is not able to resolve individual clouds, the values in Table 4 are **area** averaged column densities $\langle N \rangle$, the product between column density and area filling factor.

Column densities are converted to molecular gas mass using (see e.g., Kamenetzky et al. 2012)

$$M_{\text{region}} = \frac{m_{\text{H}_2} A_{\text{reg}} N_{\text{mol}} \Phi_A}{X_{\text{mol}}}, \quad (3)$$

where A_{reg} is the area of the region being considered, $\Phi_{A_{\text{reg}}}$ is the area filling factor of the region, m_{H_2} is the mass of an H₂ molecule, N_{mol} is the column density of the

TABLE 3
INTEGRATED LINE FLUXES IN M82

Region	S_{HCN} (Jy km s ⁻¹)	S_{HCO^+} (Jy km s ⁻¹)
Disk ^a	192 ± 4	365 ± 7
Outflow ^b	55 ± 3	112 ± 8

^a Disk area is 676 (″)² for HCN and 1011 (″)² for HCO⁺.

^b Outflow area for HCN is 940 (″)² and for HCO⁺ 1661 (″)².

TABLE 4
LOWER LIMITS TO THE COLUMN DENSITY
OUTSIDE THE CENTRAL STARBURST IN
M82.

Region	$\langle N_{\text{HCN}} \rangle$ ($\times 10^{13} \text{ cm}^{-2}$)	$\langle N_{\text{HCO}^+} \rangle$ ($\times 10^{13} \text{ cm}^{-2}$)
1	5.2 – 18.7	4.9 – 17.3 [†]
2	3.9 – 13.8	2.0 – 7.2 [†]
3	4.9 – 17.6	3.9 – 13.9 [†]
4	5.0 – 17.8	2.4 – 8.6 [†]
5	4.5 – 15.9	1.8 – 6.5 [†]
6	2.9 – 10.5 [†]	2.6 – 9.2
7	3.3 – 11.8 [†]	3.3 – 11.5
8	...	2.8 – 9.9
9	...	2.2 – 7.7
10	...	3.1 – 11.0
11	2.8 – 9.9 [†]	2.8 – 9.9
12	3.2 – 11.3 [†]	3.5 – 12.4
13	...	2.8 – 9.8
14	3.7 – 13.0 [†]	2.7 – 9.5

[†] Regions filled less than 50%.

molecule being used as mass tracer and X_{mol} abundance of this molecule with respect to H₂ ($X_{\text{mol}} = N_{\text{mol}}/N_{\text{H}_2}$). For the HCN and HCO⁺ abundances we take the values derived by Naylor et al. (2010) of $X_{\text{HCN}} \approx 7.9 \times 10^{-9}$ and $X_{\text{HCO}^+} \approx 3.9 \times 10^{-9}$, which represent an average of the abundances in the central starburst. The computed dense molecular gas masses are presented in Table 5. The lower limits are of a few $\times 10^6 M_{\odot}$, similar to the mass of a giant molecular cloud. As comparison, the mass of molecular gas inside the central starburst is $\geq 9.8 \times 10^7 M_{\odot}$ for HCN and $\geq 14 \times 10^7 M_{\odot}$ for HCO⁺, assuming optically thin emission in LTE. From this we can see that the molecular gas mass in the outflow is a factor of 10 lower than the mass in the disk. From CO observations, the mass of molecular gas in the disk is $2.3 \times 10^8 M_{\odot}$ (Walter et al. 2002). In the disk, the gas masses traced by CO, HCN and HCO⁺ seem to agree reasonably well with each other, given the large uncertainties and the differences in critical density. In the outflow the molecular mass traced by CO(1–0) is $3.3 \times 10^8 M_{\odot}$ (Walter et al. 2002). The molecular gas mass traced by HCN and HCO⁺ is $\gtrsim 2\%$ of the total molecular mass in the outflow traced by CO.

3.6. Kinematics

Moment 1 maps of the short spacings-corrected cubes are shown in Fig. 6. The moment 1 was obtained using the same masked moment technique as for the moment 0 map. The velocity of the prominent HCO⁺ emission ex-

TABLE 5
LOWER LIMITS TO THE DENSE MOLECULAR
GAS MASS OUTSIDE THE CENTRAL STARBURST
IN M82.

Region	M_{H_2} from HCN ($\times 10^6 M_\odot$)	M_{H_2} from HCO^+ ($\times 10^6 M_\odot$)
1	1.5 – 5.5	2.0 – 7.3 [†]
2	0.8 – 2.9	0.2 – 0.6 [†]
3	1.5 – 5.2	1.5 – 5.5 [†]
4	2.2 – 7.8	0.7 – 2.7 [†]
5	1.0 – 3.6	0.2 – 0.5 [†]
6	0.2 – 0.7 [†]	1.5 – 5.4
7	0.7 – 2.5 [†]	1.9 – 6.7
8	...	1.6 – 5.8
9	...	1.3 – 4.5
10	...	1.8 – 6.5
11	0.2 – 0.7 [†]	1.6 – 5.8
12	0.4 – 1.6 [†]	1.7 – 5.9
13	...	1.6 – 5.7
14	0.2 – 0.7 [†]	1.6 – 5.6
total	7.0 – 25.0	14.6 – 51.9

[†] Regions filled less than 50%. These are not considered to compute the total mass.

tending south (regions 8, 9 and 10) and north (regions 12, 13 and 14) of the central starburst is close to 232 km s^{-1} and 263 km s^{-1} respectively. After subtracting the systematic velocity of M82 (220 km s^{-1}) the velocities are 12 and 43 km s^{-1} . The wind deprojected velocity can be obtained by correcting for the outflow opening angle (55° , Walter et al. 2002) and the galaxy inclination (80° , de Vaucouleurs et al. 1991). This results in deprojected outflow velocities of ≈ 28 and $\approx 100 \text{ km s}^{-1}$. We adopt the average velocity between them, 64 km s^{-1} , as the HCO^+ outflow velocity.

For the HCN emitting gas extending north (region 5) and south (region 2) of the central starburst, the observed velocities are the same, $\approx 238 \text{ km s}^{-1}$, given our velocity resolution. This lack of velocity difference could be due to the distribution of the HCN emitting gas in the outflow. The derived deprojected outflow velocity for HCN is $\approx 43 \text{ km s}^{-1}$.

The observed velocities for the HCN and HCO^+ emitting gas do not show a blueshifted component, as observed at other wavelengths (see e.g., McKeith et al. 1995). This is consistent with emission coming from near the galactic disk in the part of the outflow closer to the observer to the north, and that farther from the observer to the south (regions II and IV in Fig. 5 of McKeith et al. 1995). Also, it is possible that the velocity of the dense molecular gas is reflecting the circular velocity it had when it was part of the molecular disk (Murray et al. 2011).

3.7. Dense gas mass outflow rate

The time it takes to the dense gas to reach its observed position outside the central starburst can be estimated from its deprojected velocity and distance from the molecular disk. The HCN emission from the outflow reaches a projected distance of $21''$, which corresponds to a deprojected linear distance of 435 pc . The HCO^+ filament to the North reaches a deprojected distance of 643 pc , and to the South of 767 pc . Given these distances and the observed gas velocity, it would

have taken $\sim 14 \text{ Myr}$ for the HCN and HCO^+ gas to reach its current location. This timescale is comparable to the age of the most recent starburst in M82 A of 5 Myr (Förster Schreiber et al. 2003), and also similar to the inferred lifetime of the SiO chimney and supershell of $\sim 1 \text{ Myr}$ (García-Burillo et al. 2001).

Using the derived values of the dense molecular gas mass in the outflow, and the time required for the gas to reach the farthest point from the $2.2 \mu\text{m}$ peak we can estimate the mass outflow rate for the dense gas, given by $\dot{M} \approx M/t$. We consider the most clear examples of outflowing dense molecular gas, regions 2, 4 and 5 for HCN, and regions 8 to 10 and 12 to 14 for HCO^+ . The total dense molecular gas mass in the mentioned HCN regions is $\geq 4 \times 10^6 M_\odot$. For HCO^+ this is $\geq 9.6 \times 10^6 M_\odot$. The dense gas mass outflow rates are then $\sim 0.3 M_\odot \text{ yr}^{-1}$ for HCN and $\sim 0.7 M_\odot \text{ yr}^{-1}$ for HCO^+ . These mass outflow rates are lower than the SFR derived from the 3 mm continuum and the mass loss rate inferred from CO observations of $33 M_\odot \text{ yr}^{-1}$ (Walter et al. 2002).

To the East of the central starburst there is a filament of HCO^+ emission. This filament originates in region 11 of Fig. 5. The velocity of this filament is lower than that of the molecular disk. This is similar to what is observed for the CO emitting gas in this region (Walter et al. 2002).

3.8. Energetics

Using the derived values for the outflow mass and velocity we can estimate the kinetic energy of the dense molecular gas outside the molecular disk. For HCN this is $\approx 4.7 \times 10^{52} \text{ erg}$, and for HCO^+ $\approx 3.2 \times 10^{53} \text{ erg}$. The source of this energy could be easily provided by the SNe explosions in M82. The energy injected to the ISM can be estimated as $\eta_{\text{inj}} \dot{N}_{\text{SNe}} E_{\text{SN}} \Delta t$, were η_{inj} is the efficiency with which a SNe transfers energy to the ISM, \dot{N}_{SNe} is the observed supernova rate, E_{SN} is the energy of a typical SNe and Δt a time interval. We assume that each SNe releases an energy of 10^{51} erg and that only 10% of it is transferred to the surrounding gas (e.g., Thornton et al. 1998). For the SNe rate we use a value of 0.04 SNe yr^{-1} inferred from the observed SNe remnants (SNR) in the starburst disk (Fenech et al. 2010). Over a timescale of 1 Myr this would supply $4 \times 10^{55} \text{ erg}$. The derived outflow energy is 0.1% of the energy provided by SNe under these assumptions. This could be caused by a lower SNe rate in the region, or a lower SNe energy injection efficiency to the dense gas.

The derived kinetic energy of the dense molecular gas is lower than that of the less dense gas traced by CO (Walter et al. 2002) by a factor of $10^2 - 10^3$. The situation is similar with respect to the kinetic energy of the ionized gas and the neutral atomic gas in the outflow. The ionized gas traced by $\text{H}\alpha$ has a kinetic energy of $2 \times 10^{55} \text{ erg}$ (Shopbell & Bland-Hawthorn 1998) and the neutral atomic gas of $(1 - 5) \times 10^{54} \text{ erg}$ (Contursi et al. 2013). The kinetic energy of the warm molecular gas is 10^{51} erg (Veilleux et al. 2009). This makes the dense cool molecular gas one of the least energetic components of the outflow.

4. SUMMARY

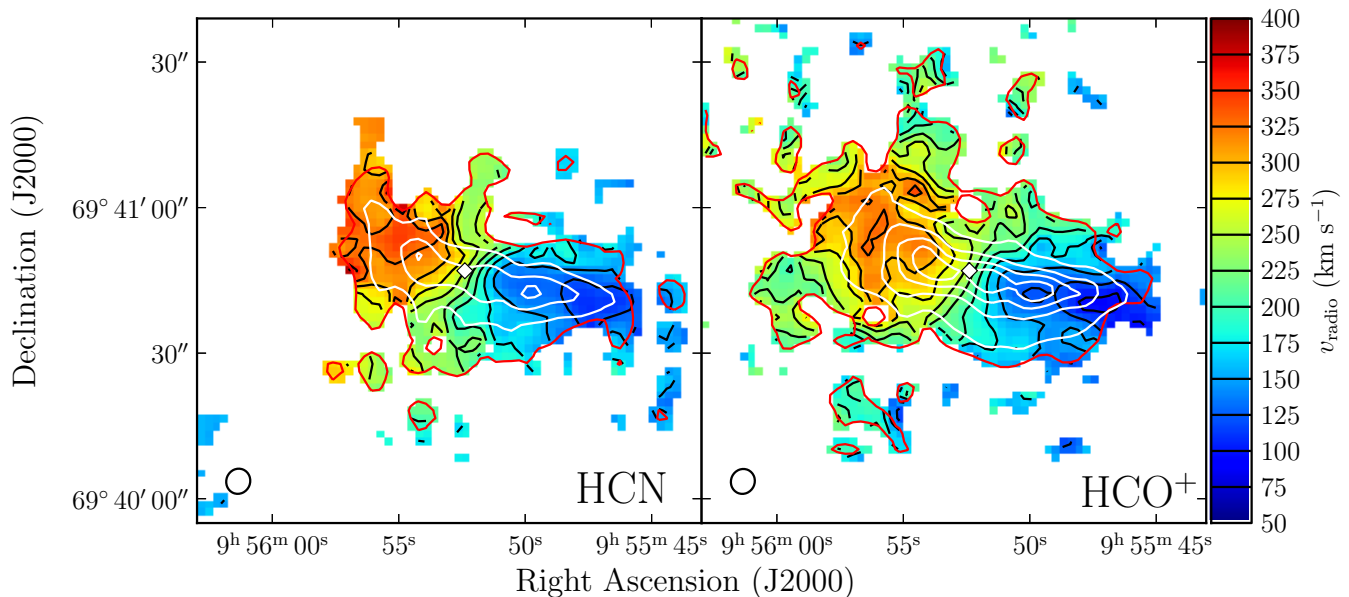


FIG. 6.— Line of sight velocity (moment 1) maps of line emission in the central starburst of M82 (black contours and color scale). The galaxy center defined by the $2.2 \mu\text{m}$ peak is shown as a white diamond (Dietz et al. 1989). The CARMA beam is shown in the lower left corner of each panel. *White* contours represent the moment 0 map and increment by 12σ .

We presented HCN and HCO^+ observations of the starburst galaxy M82. These observations are a combination of high sensitivity single dish images obtained with the GBT, and high resolution CARMA observations. They cover a region of 1.2 kpc and trace structures of size ≈ 100 pc, including the low surface brightness emission associated with the starburst-driven outflow.

The distribution and kinematics of the HCN and HCO^+ emission suggests that the gas is being blown out of the central molecular disk through at least one chimney, similar to what is observed at other wavelengths in M82. Assuming that the gas in the outflow is in LTE and optically thin we place lower limits to the mass of dense molecular gas in the outflow. Using the $\text{HCN}(1-0)$ and $\text{HCO}^+(1-0)$ lines the mass of dense gas is $\gtrsim 7 \times 10^6 M_\odot$. This is $\geq 2\%$ of the total outflow mass as traced by the CO $J = 1 - 0$ line.

The energy required to expel this amount of dense gas

from the central starburst is $(1 - 10) \times 10^{52}$ erg. This energy is about 0.1% of the total energy provided by SNE in M82.

The rate at which dense gas is being blown out of the central starburst would imply that the starburst episode would last $\geq 5\%$ less than in the absence of the outflow of dense molecular gas.

ACKNOWLEDGMENTS

We thank the anonymous referee for providing feedback which helped improve the content and clarity of this work. G. G. and P. S. acknowledge support from proyecto FONDECYT regular 1120195, proyecto Anillo ACT1102 and Basal PFB-06 CATA. A. D. B. wishes to acknowledge partial support from a CAREER grant NSF-AST0955836, NSF-AST1139998 and from NSF-AST1412419. This research made use of Astropy (Astropy Collaboration et al. 2013).

REFERENCES

- Achtermann, J. M., & Lacy, J. H. 1995, *ApJ*, 439, 163
 Aladro, R., Martín, S., Martín-Pintado, J., et al. 2011b, *A&A*, 535, A84
 Aladro, R., Martín-Pintado, J., Martín, S., Mauersberger, R., & Bayet, E. 2011a, *A&A*, 525, A89
 Astropy Collaboration, et al. 2013, *A&A*, 558, A33
 Bolatto, A. D., Warren, S. R., Leroy, A. K., et al. 2013, *Nature*, 499, 450
 Bregman, J. N., Schulman, E., & Tomisaka, K. 1995, *ApJ*, 439, 155
 Brouillet, N., & Schilke, P. 1993, *A&A*, 277, 381
 Carlstrom, J. E. 1989, PhD thesis, California Univ., Berkeley.
 Carlstrom, J. E., & Kronberg, P. P. 1991, *ApJ*, 366, 422
 Contursi, A., Poglitsch, A., Gracia Carpio, J., et al. 2013, *A&A*, 549, A118
 Dalcanton, J. J., Williams, B. F., Seth, A. C., et al. 2009, *ApJS*, 183, 67
 Dame, T. M. 2011, ArXiv e-prints
 de Vaucouleurs, G., de Vaucouleurs, A., Corwin, Jr., H. G., et al. 1991, Third Reference Catalogue of Bright Galaxies. Volume I: Explanations and references. Volume II: Data for galaxies between 0^h and 12^h . Volume III: Data for galaxies between 12^h and 24^h .
 Dietz, R. D., Gehr, R. D., Jones, T. J., et al. 1989, *AJ*, 98, 1260
 Engelbracht, C. W., Kundurthy, P., Gordon, K. D., et al. 2006, *ApJL*, 642, L127
 Fenech, D., Beswick, R., Muxlow, T. W. B., Pedlar, A., & Argo, M. K. 2010, *MNRAS*, 408, 607
 Förster Schreiber, N. M., Genzel, R., Lutz, D., & Sternberg, A. 2003, *ApJ*, 599, 193
 García-Burillo, S., Martín-Pintado, J., Fuente, A., & Neri, R. 2001, *ApJL*, 563, L27
 Helfer, T. T., Thornley, M. D., Regan, M. W., et al. 2003, *ApJS*, 145, 259
 Jura, M., Hobbs, R. W., & Maran, S. P. 1978, *AJ*, 83, 153
 Kamenetzky, J., Glenn, J., Rangwala, N., et al. 2012, *ApJ*, 753, 70
 Kepley, A. A., Leroy, A. K., Frayer, D., et al. 2014, *ApJL*, 780, L13

- Lim, S., Hwang, N., & Lee, M. G. 2013, *ApJ*, 766, 20
- Loiseau, N., Nakai, N., Sofue, Y., et al. 1990, *A&A*, 228, 331
- Lynds, C. R., & Sandage, A. R. 1963, *ApJ*, 137, 1005
- McKeith, C. D., Greve, A., Downes, D., & Prada, F. 1995, *A&A*, 293, 703
- Melioli, C., de Gouveia Dal Pino, E. M., & Geraissate, F. G. 2013, *MNRAS*, 430, 3235
- Murphy, E. J., Condon, J. J., Schinnerer, E., et al. 2011, *ApJ*, 737, 67
- Murray, N., Ménard, B., & Thompson, T. A. 2011, *ApJ*, 735, 66
- Mutchler, M., Bond, H. E., Christian, C. A., et al. 2007, *PASP*, 119, 1
- Nakai, N., Hayashi, M., Handa, T., et al. 1987, *PASJ*, 39, 685
- Naylor, B. J., Bradford, C. M., Aguirre, J. E., et al. 2010, *ApJ*, 722, 668
- Neininger, N., Guelin, M., Klein, U., Garcia-Burillo, S., & Wielebinski, R. 1998, *A&A*, 339, 737
- Nguyen, Q.-R., Jackson, J. M., Henkel, C., Truong, B., & Mauersberger, R. 1992, *ApJ*, 399, 521
- Nguyen-Q-Rieu, Nakai, N., & Jackson, J. M. 1989, *A&A*, 220, 57
- O'Connell, R. W., & Mangano, J. J. 1978, *ApJ*, 221, 62
- Ohyama, Y., Taniguchi, Y., Iye, M., et al. 2002, *PASJ*, 54, 891
- Oppenheimer, B. D., & Davé, R. 2006, *MNRAS*, 373, 1265
- Oppenheimer, B. D., Davé, R., Kereš, D., et al. 2010, *MNRAS*, 406, 2325
- Puxley, P. J., Brand, P. W. J. L., Moore, T. J. T., et al. 1989, *ApJ*, 345, 163
- Regan, M. W., Thornley, M. D., Helfer, T. T., et al. 2001, *ApJ*, 561, 218
- Remijan, A. J., Markwick-Kemper, A., & ALMA Working Group on Spectral Line Frequencies. 2007, in *Bulletin of the American Astronomical Society*, Vol. 39, American Astronomical Society Meeting Abstracts, #132.11
- Roussel, H., Wilson, C. D., Vigroux, L., et al. 2010, *A&A*, 518, L66
- Sanders, D. B., Mazzarella, J. M., Kim, D.-C., Surace, J. A., & Soifer, B. T. 2003, *AJ*, 126, 1607
- Sault, R. J., Teuben, P. J., & Wright, M. C. H. 1995, in *Astronomical Society of the Pacific Conference Series*, Vol. 77, *Astronomical Data Analysis Software and Systems IV*, ed. R. A. Shaw, H. E. Payne, & J. J. E. Hayes, 433
- Schöier, F. L., van der Tak, F. F. S., van Dishoeck, E. F., & Black, J. H. 2005, *A&A*, 432, 369
- Seaquist, E. R., Frayer, D. T., & Bell, M. B. 1998, *ApJ*, 507, 745
- Shoppell, P. L., & Bland-Hawthorn, J. 1998, *ApJ*, 493, 129
- Springel, V., & Hernquist, L. 2003, *MNRAS*, 339, 312
- Stanimirovic, S. 2002, in *Astronomical Society of the Pacific Conference Series*, Vol. 278, *Single-Dish Radio Astronomy: Techniques and Applications*, ed. S. Stanimirovic, D. Altschuler, P. Goldsmith, & C. Salter, 375–396
- Stevens, I. R., Read, A. M., & Bravo-Guerrero, J. 2003, *MNRAS*, 343, L47
- Strickland, D. K., Heckman, T. M., Colbert, E. J. M., Hoopes, C. G., & Weaver, K. A. 2004, *ApJ*, 606, 829
- Strickland, D. K., Ponman, T. J., & Stevens, I. R. 1997, *A&A*, 320, 378
- Thornton, K., Gaudlitz, M., Janka, H.-T., & Steinmetz, M. 1998, *ApJ*, 500, 95
- Tsai, A.-L., Matsushita, S., Kong, A. K. H., Matsumoto, H., & Kohno, K. 2012, *ApJ*, 752, 38
- Veilleux, S., Cecil, G., & Bland-Hawthorn, J. 2005, *ARA&A*, 43, 769
- Veilleux, S., Rupke, D. S. N., & Swaters, R. 2009, *ApJL*, 700, L149
- Walter, F., Weiss, A., & Scoville, N. 2002, *ApJL*, 580, L21
- Weiß, A., Walter, F., & Scoville, N. Z. 2005, *A&A*, 438, 533
- Wills, K. A., Redman, M. P., Muxlow, T. W. B., & Pedlar, A. 1999, *MNRAS*, 309, 395
- Yamagishi, M., Kaneda, H., Ishihara, D., et al. 2012, *A&A*, 541, A10
- Yamaguchi, Y., Richards, Jr., C. A., & Schaefer, III, H. F. 1994, *J. Chem. Phys.*, 101, 8945